International Journal of Civil Engineering
https://doi.org/10.1007/s40999-024-01002-y

RESEARCH PAPER

Study on Seismic Performance of Precast Shear Wall Structure Connected by Sleeve and Threaded Rod Connectors

Tianxi Cheng[1] · Shuo Li[1] · Yunyan Bai[1] · Peijun Wang[1] · Qi Wang[2] · Jie Song[3] · Mei Liu[1]

Received: 23 June 2023 / Revised: 20 April 2024 / Accepted: 4 June 2024

Abstract

Two precast shear walls connected by sleeve and high-strength threaded rod connectors and a precast shear wall connected by grouting sleeves were tested under cyclic loading. The results show that, compared with the precast shear wall connected by the grouting sleeve, the ductility of the new type of shear wall increased by 16.7%, the energy dissipation capacity decreased by 3%, and the bearing capacity and stiffness degradation ability were similar. A finite element parameter analysis was conducted, studying the effects of the axial compression ratio and shear span ratio on the performance of the new type of precast shear wall. The results show that as the axial compression ratio increased from 0.1 to 0.3, the bearing capacity increased by 21.8%, and the peak load displacement decreased by 36.1%. As the shear span ratio increased from 1.09 to 1.82, the failure mode of the specimen showed a trend of changing from shear-compression failure to bending failure. In addition, based on the experimental results and simulation results, a calculation formula for the lateral bearing capacity of shear walls has been proposed, providing a basis for the design of new types of shear walls.

Keywords Precast shear wall · Sleeve and threaded rod connectors · Finite element parametric analysis · Seismic performance

1 Introduction

Prefabricated concrete structures have received more and more attention due to their high quality, fast construction speed, material saving, and reduction of construction waste [1]. The rapid manufacturing and mechanized assembly of prefabricated concrete structural elements present significant advantages in terms of reducing on-site labor requirements and enhancing construction efficiency, which has positive economic, social, and environmental impacts. [2].

In the prefabricated structural system, the prefabricated shear wall offers significant advantages in terms of lateral stiffness and load-bearing capacity [3], which makes the prefabricated shear wall become the focus of many scholars' research. To ensure the stable performance and integrity of the structure, the joint between precast shear walls has become an important factor restricting the development of prefabricated shear walls [4]. The joint splices the lower and upper or the left and right prefabricated shear walls into a whole so that the adjacent shear walls and floor slabs can form a whole to bear wind loads

✉ Peijun Wang
pjwang@sdu.edu.cn

Tianxi Cheng
1191445624@qq.com

Shuo Li
3263540245@qq.com

Yunyan Bai
by520725@163.com

Qi Wang
qiwangcumt@163.com

Jie Song
jiesonggdue@163.com

Mei Liu
liumei@sdu.edu.cn

[1] School of Civil Engineering, Shandong University, Jinan 250061, Shandong, China

[2] State Key Laboratory for Geo-mechanics and Deep Underground Engineering, China University of Mining and Technology, Beijing 100083, China

[3] Building Research Academy of Shandong, Jinan 250061, Shandong, China

Published online: 15 June 2024

and earthquakes together. Therefore, the performance of the joints determines the overall performance of the building structure to a certain extent [5]. Numerous scholars have conducted extensive research on the connections of prefabricated shear walls [6, 7].

At present, the connection methods of prefabricated shear walls are increasing, forming a connection system including wet joints and dry joints. The wet joint of prefabricated shear walls includes grout anchor connection, grouting sleeve connection [8], etc. Peng et al. [9] studied the performance of precast concrete shear walls using mortar-sleeve connections. The results revealed that the mortar-sleeve connection can effectively transfer the loads between the shear walls. Xu et al. [10] studied the seismic behavior of precast shear walls connected by single-row grouted sleeves. The experimental results showed that precast shear wall specimens were comparable to cast-in-place shear wall specimens in terms of bearing capacity, energy dissipation capacity and ductility. Zhi et al. [11] compared the performance of prefabricated shear walls connected by metal bellows grouted connections and cast-in-place shear walls. The results show that the prefabricated shear walls connected by metal bellows grouted connections exhibit good load-bearing capacity and energy dissipation capacity.

These studies [9–11] show that the grouting wet joint of prefabricated shear walls can be comparable to the cast-in-place connection to a certain extent, but this connection method also has certain shortcomings. There is uncertainty in grouting sleeve connections. During the grouting process, the mortar was prone to backflow, resulting in partially grouted or completely ungrouted sleeves, which greatly affected the joint performance of the precast shear walls [12]. Some scholars [13] studied the effect of sleeve grouting defects on the seismic performance of prefabricated shear walls, showing that grouting sleeve defects seriously affect the load-bearing capacity of shear wall structures.

The dry joint is also an important part of the prefabricated structure connection. Dry joints of the precast shear wall (especially bolted connections) are easy to install and save a lot of manpower and material resources, which makes it attractive in practice. Some scholars have also done some research which is about the dry joint of prefabricated shear walls. The dry joint of prefabricated shear walls includes bolted connection [14, 15], welded connection [16, 17], etc. El Semelawy et al. [18, 19] presented an innovative prefabricated wall connection technique using threaded steel anchor bolts and conducted experiments on four scaled-down models, which showed good ductility of the connection. Guo et al. [20] investigated the seismic performance of precast shear walls connected by high-strength bolts, showing that precast shear walls with this type of dry connection exhibited good energy dissipation capacity and seismic ductility. Li et al. [21] investigated four scaled-down prefabricated shear wall models connected by the bolt-plate connection The results show that the load-carrying capacity of the precast shear walls using this new dry connection is comparable to that of cast-in-place shear walls. Han et al [22] proposed a method of steel plate bolt connection for prefabricated shear walls and conducted experimental research on five shear wall specimens. The experimental results show that this connection method can provide effective strength and stiffness for the shear wall system. Based on Han's research, Naserpour et al. [23] further proposed a shear wall assembled from slender walls, and the research shows that this kind of shear wall has higher ductility.

Different dry connection methods reflect different connection performances. Based on the above research [18–23], it can be found that the reasonable dry joint of the shear wall can effectively transmit vertical force, shear force and bending moment between shear walls, and that the seismic performance of prefabricated shear walls can be similar to that of cast-in-site components. However, the above research also exposed a problem with dry joints. These types of dry joints do not pay attention to the connection of the reinforcing steels between the interconnected prefabricated shear walls, which makes the integrity of the connection of the components insufficient.

To address the drawbacks of existing joints and simplify the composition of prefabricated joints, this study proposes the sleeve and threaded rod connector (STRC) consisting of a double sleeve connector, a threaded sleeve, and a high-strength threaded rod. The details and specific composition of the connector are shown in Fig. 1. During the fabrication of precast components, the ends of the longitudinal connecting steel bars of the upper precast shear wall (PSW) are threaded and connected to the double sleeve connectors via threads. The double sleeve connectors are embedded in the upper PSW and hand holes are reserved at the corresponding positions in the wall. The ends of the longitudinal connecting steel bars of the lower PSW are threaded and connected to the threaded sleeves via threads. The threaded sleeves are embedded in the lower PSW. When connecting the PSW, one end of the high-strength threaded rod is connected to the threaded sleeve of the lower PSW, the other end passes through the reserved hole in the floor slab and the non-threaded sleeve of the double sleeve connector, and is fixed with a nut. Finally, the hand holes are filled with mortar, completing the installation of the PSW. Three specimens were tested under cyclic loading behavior, one specimen connected by grouting sleeves and two specimens connected by STRCs. This paper focuses on the experimental phenomena, strength, energy dissipation capacity, ductility, and stiffness degradation of the PSW

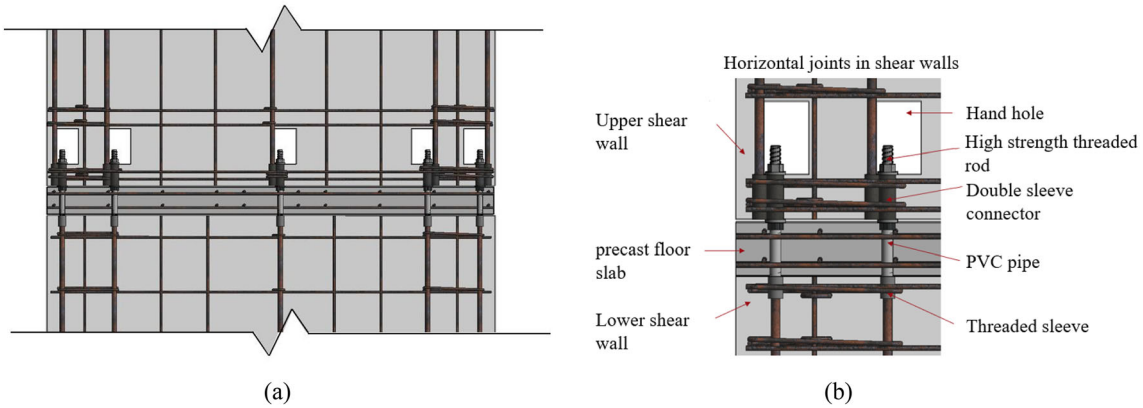

Fig. 1 Sleeve and threaded rod connection: **a** Horizontal joint connection of shear wall; **b** Connection details

using the new joints. Furthermore, finite element analysis was conducted on the PSWs connected by this novel dry joint to investigate the influence of parameters such as axial compression ratio and shear span ratio on the performance of the novel PSW. Finally, the lateral bearing capacity calculation formula of the PSW is proposed.

2 Experimental Program

To investigate the seismic performance of precast shear walls(PSWs) using the STRC, three full-scale PSWs were fabricated, including two prefabricated specimens connected by the STRC and one prefabricated specimen connected by grouted sleeves. The comparison of these three specimens reflects two variables which are the type and the number of connectors. During the test, the samples were loaded with both vertical compression and horizontal cyclic reciprocating loads, and corresponding data was finally obtained through reasonable measurement methods.

2.1 Test Specimens

The specimen consists of an upper PSW, a lower PSW, foundation beams and two floor slabs. The dimensions, reinforcement arrangement, section details and connector locations of the three specimens are given in Fig. 2. The prefabricated shear wall is divided into two side construction column parts and a middle part. The longitudinal connecting steel bars of the construction column part form the steel mesh of the construction column, and the position of the connectors is determined according to the position of the longitudinal connecting steel bars. The connectors in the middle part are arranged in a uniformly distributed manner. The vertical connecting bars are hot-rolled ribbed third-grade threaded bars with a diameter of 16 mm. The vertical non-connecting steel bars are hot-rolled ribbed third-grade threaded steel bars with a diameter of 8 mm. The specific distribution of steel bars is given in Fig. 2.

Three test specimens have the same design in terms of dimension, but differ from each other in connection details. The other component parameters are given in Table 1. The number of connectors for both PWF1 and PWF2 is 12, but the types of connectors are different. The type of connector for specimen PWF1 is the grouted sleeve and the type of connector for specimen PWF2 is the STRC. Specimens PWF2 and PWF3 have the same types of connectors, but the number of connectors is different. The number of connectors for specimen PWF2 is 12, and the number of connectors for specimen PWF3 is 10.

2.2 Material Properties

The concrete material properties tests were carried out on three 150 mm × 150 mm × 150 mm cubes, following the Chinese standard [24]. The compressive strength of concrete cubes f_{cc}, average compressive strength of concrete cubes f_{cu}, the standard value for axial compressive strength of concrete f_{ck}, and design value of compressive strength of axial cores f_c were obtained in accordance with the standard [25], and their specific values are shown in Table 2. The filling material for the construction handholes and the grout for the grout sleeves were similarly tested. The test results show that the compressive strengths of the filling mortar for the hand holes and the grout for the grout sleeve after curing are 73 MPa and 110 MPa, respectively, which meet the requirements of relevant specifications [26]. Material properties of reinforcement, double sleeve connectors (Q235), and high-strength threaded rods were obtained through experiments according to the Chinese standard [27]. The specific values are shown in Table 3.

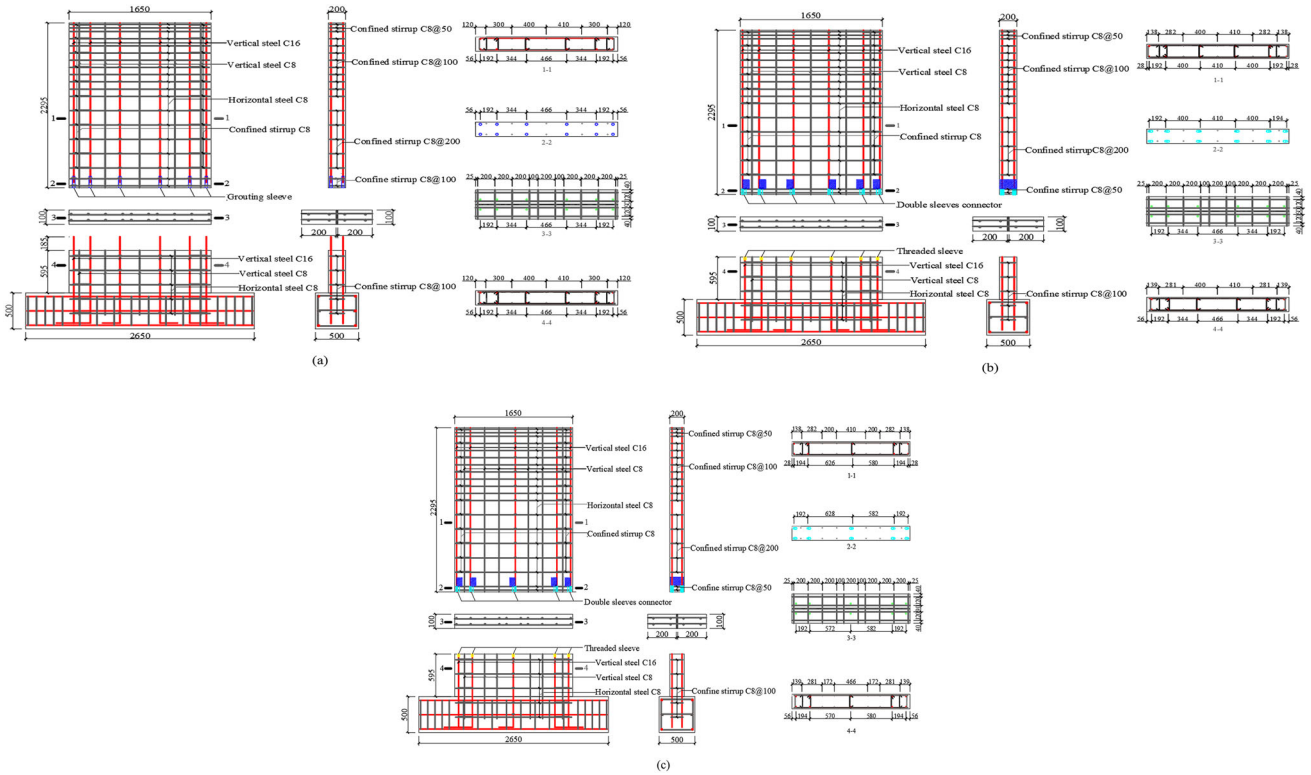

Fig. 2 Design diagram of test specimens: **a** PW1; **b** PW2; **c** PW3

Table 1 Parameters of the three specimens

Specimen	parameter			
	Type of connector	Number of connectors	Number of construction hand holes	Ratio of reinforcement
PWF1	Grouting sleeve	12	-	0.88%
PWF2	STRC	12	6	0.88%
PWF3	STRC	10	5	0.88%

Table 2 Compressive strength of concrete

Specimens	Grade	f_{cc}(MPa)	f_{cu}(MPa)	f_{ck} (MPa)	f_c (MPa)
CB1	C30	32.2	34.2	22.87	
CB2	C30	34.2			16.34
CB3	C30	35.7			

Table 3 Material Properties of Steel Materials

Steel type	Diameter (mm)	Modulus of elasticity *Es* (GPa)	Average yield stress f_y (MPa)	Average ultimate stress f_u (MPa)
HRB400	8	200	428.4	590.2
HRB400	16	200	416.6	573.8
Q235	–	206	277.9	392.6
8.8 grade threaded rod	–	232	623	796

2.3 Test Setup and Loading Procedure

The specimens with different connection details were tested on the reaction frame shown in Fig. 3. The lower beam of the specimen was held on the floor of the reaction frame by the anchor bolts. Along the length of the lower beam, an external force was applied to the lower beam by a jack on one side, while the other side was blocked by a fixture to restrain the specimen from sliding horizontally. The horizontal low-cycle reciprocating load was applied using an actuator of 2500 KN. The vertical force was loaded on top of the test piece using a hydraulic jack of 1000 kN. Horizontal sliding devices are installed at the top and bottom of the hydraulic jacks to ensure that the vertical force on the specimen is always vertically downward.

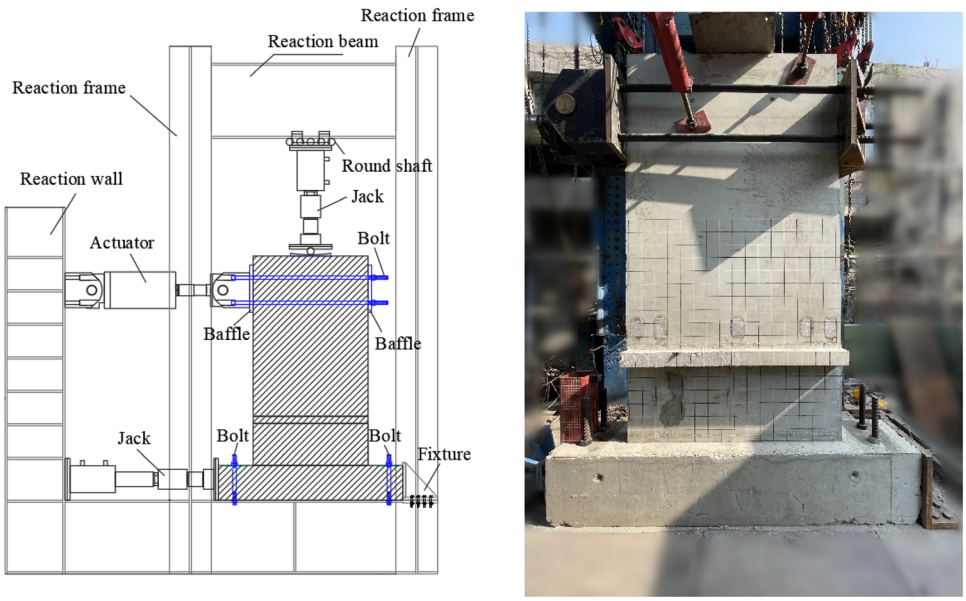

Fig. 3 Description of specimen test position: **a** Diagram of specimen testing; **b** Photograph of specimen testing

Linear variable displacement transducers (LVDTs) were used in the test to obtain data on horizontal displacement and sliding of the upper PSW. The specimens were equipped with four LVDTs, and their position distribution is shown in Fig. 4. The LVDT-1 was located 1800 mm from the underside of the upper PSW and measured the displacement at the point where the horizontal load was applied. The LVDT-2 was located 50mm from the underside of the upper PSW and measured the displacement of the lower part of the upper PSW. The LVDT-3 was located 50 mm from the underside of the floor slab and measured the displacement of the floor slab. The LVDT-4 was located 250 mm from the underside of the lower beam and measured the slip between the ground and the lower beam. The strain gauges measured the strain in the longitudinal reinforcement, and their locations are given in Fig. 4.

In the test, a vertical axial force of $0.1f_cA_c/1.2$ was applied through a jack first, f_c is the design value for the axial compressive strength of concrete, A_c indicates the value of the cross-sectional area of the wall, and the applied vertical force is calculated to be 442kN. The horizontal cyclic loads of the PSWs were then loaded according to seismic test specification [28]. Before applying the horizontal load, it is necessary to perform a preloading test on the specimen and observe the curve shape to determine if there are any installation defects. If

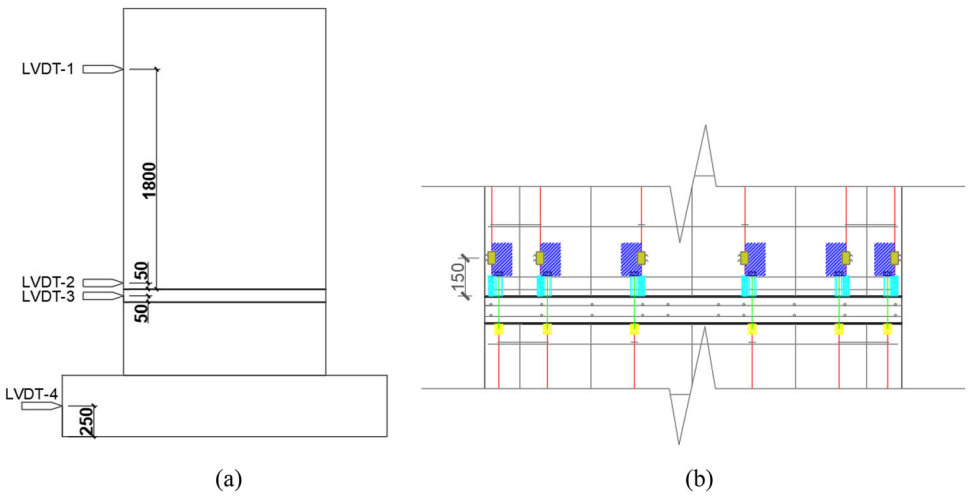

Fig. 4 Layout diagram of measuring device: **a** Layout diagram of LVDTs; **b** Layout diagram of strain gauges

the curve is normal, the horizontal load can be applied formally. As illustrated in Fig. 5, the horizontal loading scheme includes two phases: the force-controlled loading phase and the displacement-controlled phase. The force-controlled phase was to load step by step with a difference of 20 kN, and Each load was loaded back and forth for one cycle until the specimen cracked. In the displacement-controlled phase, the displacement of the cracking point of the specimen is measured as the difference between the two steps. The loading process is carried out step by step, and the displacement of each level is reciprocated for three cycles, until the specimen's bearing capacity decreases to 85% of the peak bearing capacity. At this point, the test is considered complete.

3 Experimental Results and Discussion

3.1 Crack Distribution and Failure Modes

The distributions of cracks for each PSW are illustrated in Fig. 6. When the horizontal load reaches 180 kN, the displacement of specimen PWF1 measured by LVDT1 is 6 mm. At this load level, the first crack appears, positioned 300 mm above the bottom of the upper PSW, marking the initiation of the cracking phase. As the test progresses, minor cracks start to appear on the lower side of the upper PSW and the upper side of the lower PSW. These cracks gradually extend diagonally at a 45° angle, with their width continuously increasing. When the displacement of the PWF1 exceeds 24 mm, the horizontal joint between the floor slab and the upper PSW cracks, and the width increases continuously. Additionally, the concrete on the upper two corners of the lower PSW is severely cracked. When the displacement reaches 5 times the cracking displacement and the displacement of the upper PSW reaches 30 mm, the width of the horizontal joint between the floor slab and the upper PSW further increases, and the concrete starts to detach from the upper two corners of the lower PSW. The bearing capacity of PWF1 decreases to 85% of its maximum bearing capacity, marking the end of this test.

When the horizontal load reaches 220 kN, the displacement of specimen PWF2 measured by LVDT1 is 8mm. At this load level, small cracks emerge on the edges of the construction hand holes located on the right and left sides of the upper PSW, marking the initiation of the cracking phase. As the PWF1 specimen test progresses, additional small cracks appear sequentially on the lower side of the upper PSW, along the right and left sides of the floor, and on the upper side of the lower PSW. These cracks propagate downward at a 45° angle. When the displacement exceeds 32 mm, the concrete on the left side of the floor slab becomes crushed and falls off, exposing the connected threaded rod on the edge of PWF2. When the displacement of the PWF2 reaches 40 mm, the concrete at the two corners of the lower side of the upper PSW is crushed and detached. Subsequently, the bearing capacity of PWF2 decreases to 85% of its peak bearing capacity, marking the end of this test.

When the horizontal force reaches 180 kN, the displacement of specimen PWF3 measured by LVDT1 is 6mm. At this load level, small cracks appear on the edges of the construction hand holes located on the right and left sides of the upper PSW, as well as near the horizontal joint between the floor slab and the upper PSW, indicating the onset of the cracking stage. As the displacement increases, tiny cracks appear successively in the lower part of the upper PSW, on both sides of the floor slab, and on the upper side of the lower PSW. Most of these cracks propagate downward at a 45° inclination. When the displacement approaches 24 mm, the concrete at the two corners of the lower side of the upper wall is crushed and falls off, exposing some STRCs. When the displacement of the specimen reaches 30 mm, the concrete on the left side of the lower PSW is crushed and detached. Subsequently, the bearing capacity of PWF3 decreases to 85% of its maximum bearing capacity, marking the end of this test.

As shown in Fig. 6, the damage patterns of PWF1-PWF3 are essentially the same. The steel bars on the right and left sides of the upper PSW yield in tension. Some cracks are present below half of the height of the upper wall and in the lower wall area, while the concrete near the horizontal joint is crushed and falls off. Different from PWF1, the cracks in PWF2 and PWF3 initially appear at the construction hand holes of the upper wall, and they gradually propagate during the later stage, leading to the crushing and spalling of concrete at the left and right corners of the upper PSW, and exposing the side connectors. PWF1 is cracked at the horizontal joints and the cracks at the end of the floor slab and at the lower PSW develop gradually, resulting in crushed concrete spalling at

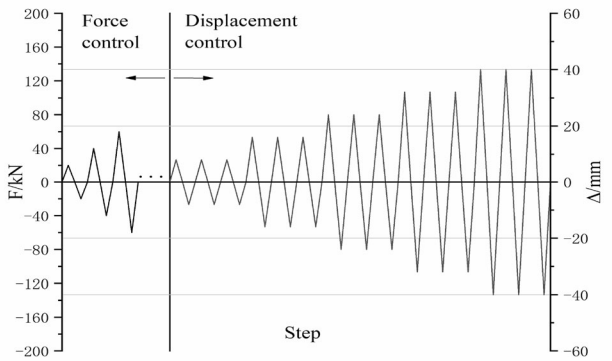

Fig. 5 Loading scheme

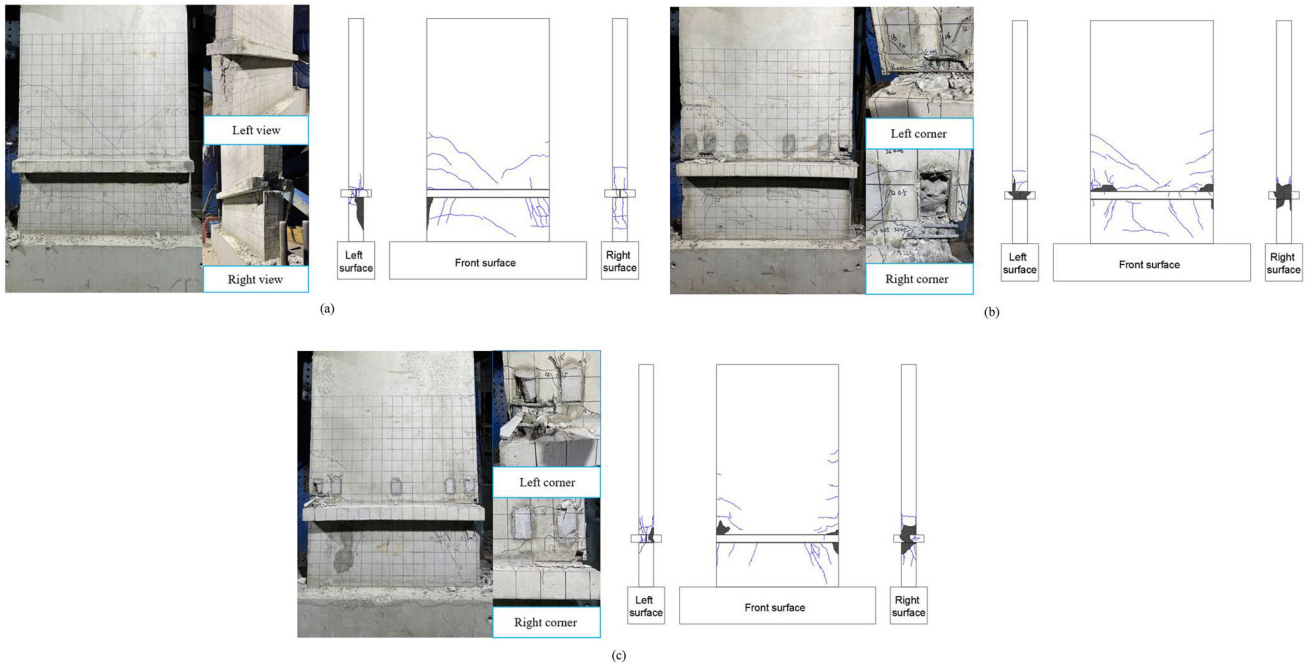

Fig. 6 Failure phenomenon and crack distribution of PWF1-PWF3: **a** PWF1; **b** PWF2; **c** PWF3

the end of the floor slab and at the right and left sides of the lower PSW.

Figure 7d, e respectively show the failure conditions of the leftmost STRC of specimens PWF2 and PWF3 after the experiment. The lower threaded rod of the STRC connector of PWF2 showed slight bending, while the upper connecting steel bar showed a slight bending and necking phenomenon. The upper connecting steel bar of the STRC connector of PWF3 only showed a slight necking phenomenon. In summary, the ductile deformation occurred in the STRC connectors of both PWF2 and PWF3, and no brittle failure occurred. This indicates that the reliability of STRC is high, and the connection meets the actual requirements of engineering.

Fig. 7 Failure conditions of connector: **a** The leftmost connector of PWF2; **b** The leftmost connector of PWF3.

3.2 Hysteresis Curves and Envelope Curves

As given in Fig. 8, the hysteresis curve of PWF1 connected by the grouting sleeve is plump. As the load approaches its peak, the load-carrying capacity decreases rapidly as the test continues. The hysteresis curve of PWF2 demonstrates a similar level of plumpness as PWF1, indicating that PWF2 possesses good energy dissipation capability. After PWF2 yields, the hysteresis curve does not show obvious shrinkage as the displacement increases, and its shape is bow-shaped. As the load-carrying capacity of specimen PWF2 approaches its peak, its bearing capacity is maintained or slowly decreases with increasing loading displacement. Compared with PWF2, the plumpness of specimen PWF3 was similar. However, the pinch phenomenon of the hysteresis curve of PWF3 is obvious, indicating that there is a certain relative sliding between the floor slab and the upper wall of specimen PWF3. This slight slippage is mainly due to the fewer number of connection nodes. After PWF3 reaches its peak load, its bearing capacity decreases slowly with the increase in displacement, indicating that it has stable structural performance and will not undergo brittle failure.

The envelope curves of PWF1-PWF3 before yielding are basically the same, showing that the initial stiffness of

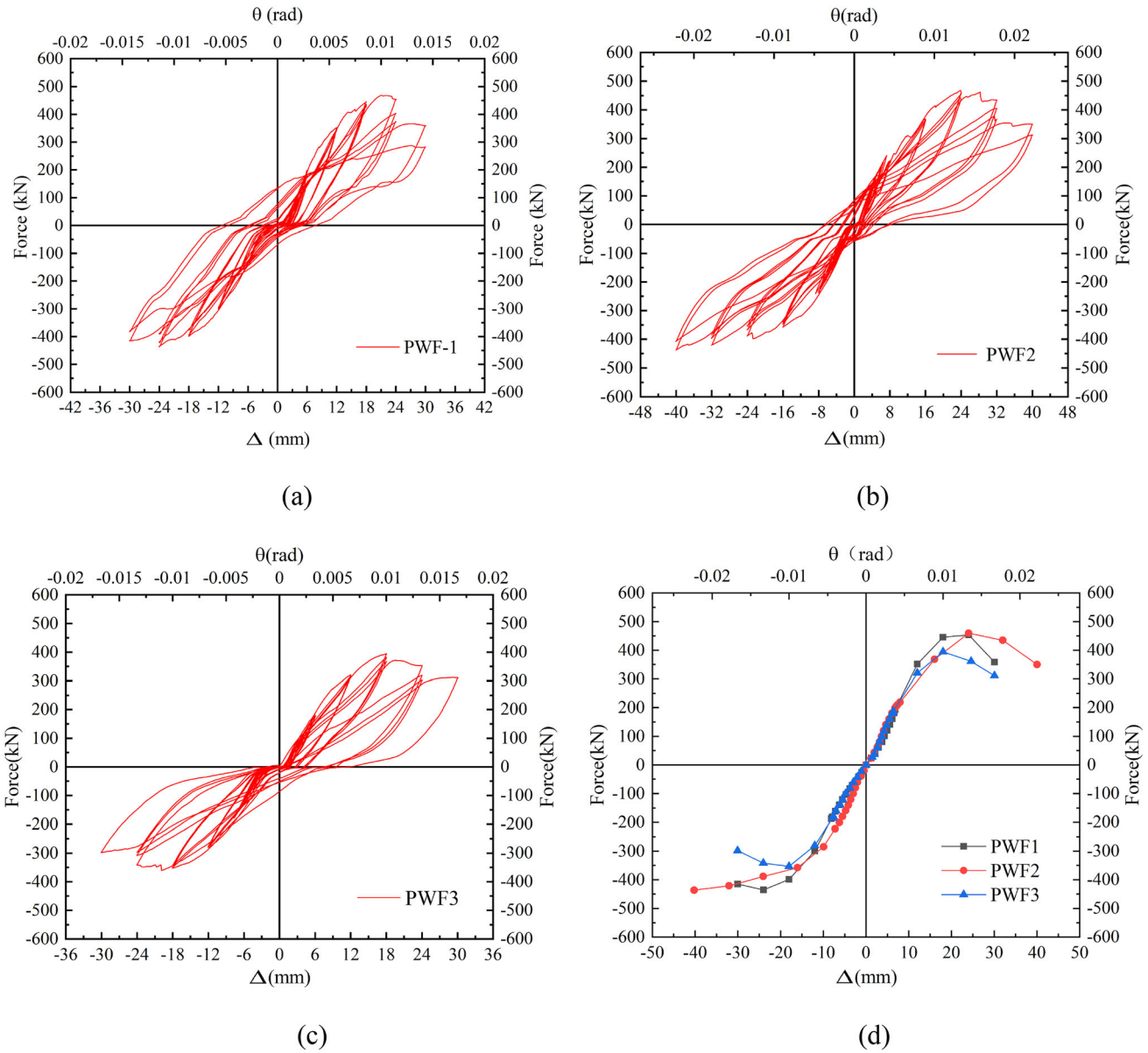

Fig. 8 Hysteresis curves and envelope curves **a** Hysteresis curve of PWF1; **b** Hysteresis curve of PWF2; **c** Hysteresis curve of PWF3; **d** Envelope curve of the test specimen

PWF1-PWF3 is essentially identical, but the displacement of PWF2 at yield is larger than that of PWF1 and PWF3. After the specimen yields, the ultimate load values of PWF1 and PWF2 are similar, but the displacement of PWF2 when the ultimate load is obtained is larger than that of PWF1. After the specimens reached the peak load, the load-carrying capacity of PWF2 and PWF3 decreased slowly, and the load-carrying capacity of PWF1 decreased rapidly.

3.3 Bearing Capacity

Table 4 presents the pertinent data concerning the load-carrying capacity of PWF1-PWF3. The yield point of each specimen is determined using the equivalent elastic-plastic energy method. The ultimate failure load (F_u) is defined as 85% of the peak load (F_p), while the yield load of the member is denoted by F_y.

The peak load of PWF1 connected by grouting sleeves and PWF2 connected by STRCs is similar, about 450kN.

Table 4 Test results

Specimen	PWF1			PWF2			PWF3		
Direction	+	−	Av	+	−	Av	+	−	Av
F_{cr}/kN	180.73	180.89	180.81	220.53	221.033	220.78	179.32	180.31	179.81
F_y/kN	387.55	366.85	377.20	361.23	357.91	359.57	317.69	328.80	323.25
F_p/kN	468.38	436.64	452.51	468.33	437.90	453.12	394.68	353.13	373.91
Δ_{cr}/mm	6.01	7.04	6.525	7.26	8.70	7.98	6.10	7.67	6.89
θ_{cr}/%	0.33	0.39	0.36	0.40	0.48	0.44	0.34	0.43	0.39
Δ_y/mm	13.29	14.42	13.86	15.46	16.23	15.85	11.82	12.69	12.26
θ_y/%	0.74	0.86	0.80	0.86	0.90	0.88	0.66	0.71	0.69
Δ_p/mm	21.10	24.01	22.56	23.91	40.04	31.98	18.03	18.04	18.04
θ_p/%	1.17	1.33	1.25	1.33	2.24	1.79	1.00	1.00	1.00
Δ_u/mm	28.12	30.03	29.18	36.19	40.22	38.20	27.39	29.80	28.60
θ_u/%	1.57	1.67	1.62	2.01	2.23	2.12	1.52	1.66	1.59
μ	2.12	2.08	2.10	2.34	2.48	2.41	2.32	2.35	2.34

This shows that the connection effect of the STRC is similar to that of the grouting sleeve connector, and the STRC can effectively connect the PSWs and transmit the shear force and bending moment between PSWs. Compared with specimen PWF2, the peak load of PWF3 is reduced by about 17.5%. This indicates that determining the appropriate quantity of STRC has a significant influence on the load-carrying capacity of the PSW.

3.4 Ductility

The yield displacement Δ_y, yield displacement angle θ_y, peak displacement Δ_p, peak displacement angle θ_p, ultimate displacement Δ_u, ultimate displacement angle θ_u and displacement ductility ratio μ of PWF1-PWF3 are given in Table 4.

In terms of the ultimate displacement angle, PWF2 has a larger ultimate displacement angle than PWF1 and PWF3. The ultimate displacement angles of PWF1 and PWF3 are similar and are about 1.6%. According to the data provided in Table 4, all the specimens exhibit displacement ductility ratios exceeding 2. The displacement ductility ratios of PWF2 and PWF3 are both larger than that of the specimen PWF1, showing that the PSWs connected with STRCs have nice deformation ability, and their ductility is better than that of PSW connected by the grouting sleeve.

(Note: The displacement ductility ratios of PWF1-PWF3 are generally small, which is due to the following reasons. (1) The height of the upper wall is less than the height of a complete PSW, which leads to the fact that the height of the horizontal load loading point is much smaller than the height of a complete PSW, and the shear span is relatively small, resulting in a small displacement ductility ratio. (2) The floor slab is added between the PSWs. The floor slab is easily damaged by compression, which causes the ultimate failure displacement of the specimens to be small, resulting in a small ductility coefficient.)

3.5 Stiffness Degradation and Strength Degradation

The specimens' stiffness degradation coefficients and strength degradation coefficients are calculated using formulae (1) and (2). The load values for the positive and negative peak points of the *i*th cycle are respectively represented as $+F_i$ and $-F_i$. The displacement values for the positive and negative peak points of the *i*th cycle are respectively represented as $+X_i$ and $-X_i$. The load value at the peak point of the *i*th cycle when the jth level load is loaded is denoted by F_j^i. The load value at the peak point of the *(i-1)*th cycle when the *j*th level load is loaded is denoted by F_j^{i-1}.

$$K_i = \frac{|+F_i| + |-F_i|}{|+X_i| + |-X_i|} \tag{1}$$

$$\lambda_i = \frac{F_j^i}{F_j^{i-1}} \tag{2}$$

Figure 9a displays the stiffness degradation curves of PWF1-PWF3. Compared with PWF1, the stiffness degradation of PWF2 and PWF3 is continuous and uniform, and the trends are stable, showing that specimens connected with the STRC have stable mechanical performance. Compared with PWF3, the stiffness degradation rate of PWF2 is higher. This is because the number of longitudinal connecting bars of PWF2 is larger than that of PWF3,

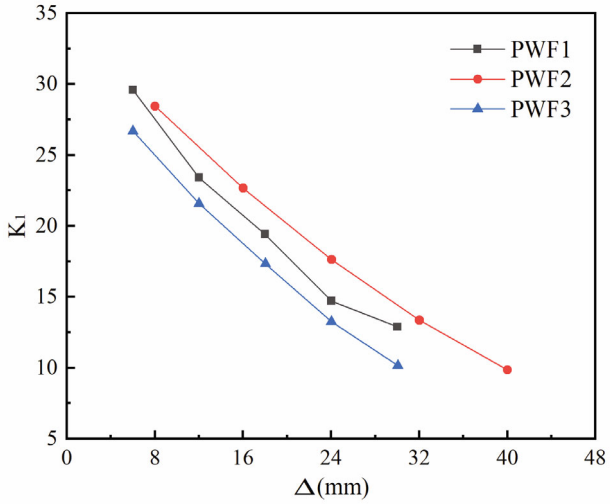

(a) Stiffness degradation curves

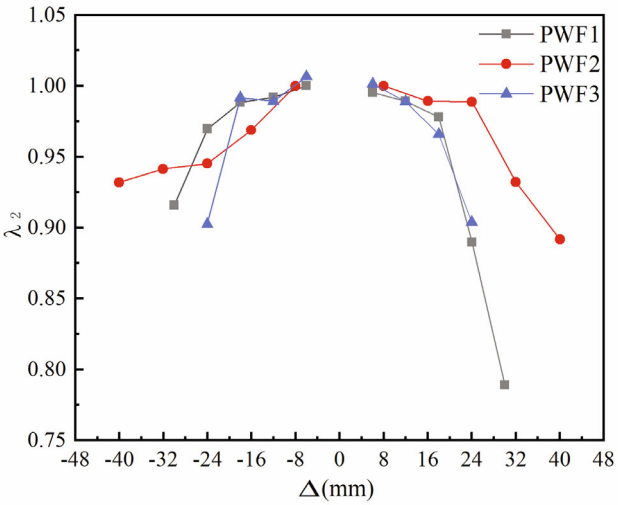

(b) Strength degradation curves

Fig. 9 Stiffness degradation curves and Strength degradation curves

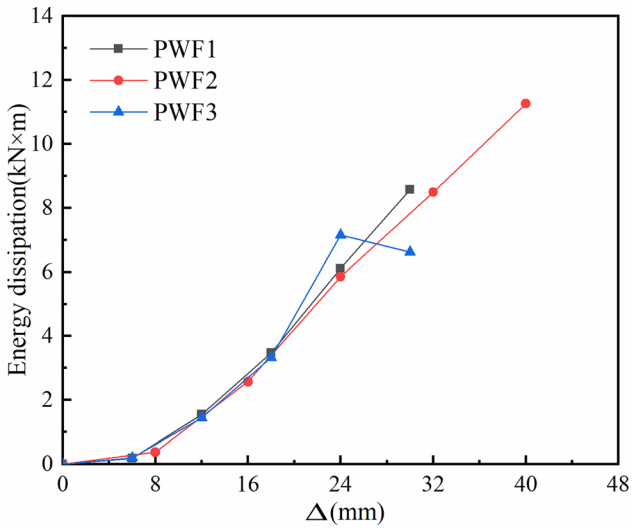

Fig. 10 Energy dissipation of PWF1-PWF3

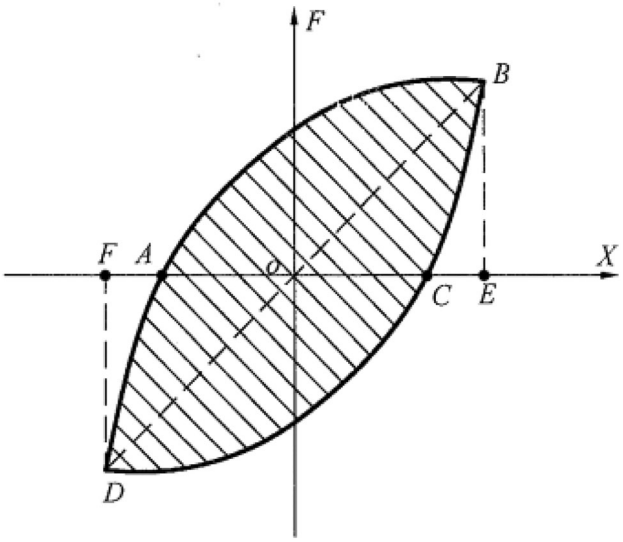

Fig. 11 Example of load-displacement hysteresis curve [28]

which makes the initial stiffness of PWF2 larger. However, PWF2 and PWF3 have similar stiffness at the ultimate failure load.

Figure 9b displays the strength degradation curves of PWF1-PWF3. PWF2 and PWF3 have a small variation range of positive and negative strength degradation, and are relatively symmetrical, indicating that the positive and negative strength performance of the specimens connected by STRCs is stable. When the last two levels of load were applied, the forward strength of the specimen PWF1 degraded rapidly. This is because in the last two stages, the horizontal crack in the specimen PWF1 widened severely, resulting in the faster degradation of PWF1's forward strength.

3.6 Energy Dissipation Capacity

The curve depicted in Fig. 10 illustrates the energy dissipation of PWF1-PWF3 at various levels of the horizontal loading displacement. As the displacement increases, each specimen's ability to dissipate energy rises gradually. Prior to reaching the yielding displacement, the curves of PWF1-PWF3 overlap. After the yield point, however, the plastic deformation capacity of PWF3 increases, leading to a faster rate of energy dissipation and a gradual deviation of its curve from the others. Once PWF3 reaches its peak load, the energy dissipation gradually decreases. Although the energy dissipation curves of PWF1 and PWF3 are similar,

Table 5 Energy dissipation factor E of specimens

specimen	Cracking load phase	Yielding load phase	Ultimate load
PWF1	0.20	0.42	0.74
PWF2	0.20	0.44	0.71
PWF3	0.22	0.40	0.71

the greater deformation capacity of PWF2 allows its energy dissipation curve to continue increasing after PWF1 reaches its ultimate failure displacement.

A specimen's energy dissipation capacity can be evaluated by the energy dissipation factor E[28]. The energy dissipation factor E is obtained from formula (3). In formula (3), $S_{(ABC+CDA)}$ is the area inside the load-displacement curve given in Fig. 11, and $S_{(OBE+ODF)}$ is the sum of the areas of the triangles OBE and ODF shown in Fig. 11.

$$E = \frac{S_{(ABC+CDA)}}{S_{(OBE+ODF)}} \tag{3}$$

Table 5 shows that the energy dissipation factors of PWF1-PWF3 at each stage are basically the same, illustrating the energy dissipation capacity of PSW connected by STRCs is similar to that of PSW connected by grouted sleeves.

4 Finite Element Analysis

4.1 Finite Element(FE) Modeling

Figure 12 shows the model of PSW connected by the STRC, established using Abaqus software. The PSW, foundation beam and double sleeve connector are modeled using eight-node reduced integration hexahedral solid elements (C3D8R). The steel reinforcement and threaded rods are modeled using two-node three-dimensional truss elements (T3D2). The mesh size of the PSW, floor slabs, and foundation beam is 50mm, while the mesh size of the double sleeve connectors and nuts is 8mm. The mesh size of the steel reinforcement and threaded rods is 50mm.

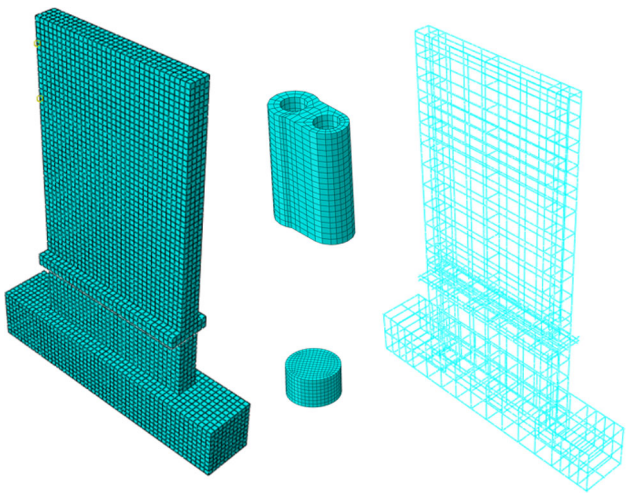

Fig. 12 Finite element model of specimens

The concrete material properties are simulated using the Concrete Damage Plasticity (CDP) model, with compressive and tensile parameters of concrete determined in accordance with the standard GB50010-2010 [25]. This model can effectively simulate the damage of the PSW. Steel reinforcement and other steel materials are simulated using a bilinear model.

Steel reinforcement and connectors are embedded in concrete. The contact between PSW and the floor slab is simulated using a surface-to-surface contact approach. In the tangential direction, the friction model is employed with a friction coefficient set to 0.3, while a hard contact model is utilized in the normal direction. The boundary conditions of the model are the displacement constraints of the x, y, and z axes of the base of the restrained beam.

In the reference. [29], the skeleton curves obtained by the monotonic loading method for the same samples are similar in shape to those obtained by cyclic loading tests. Although some index values are slightly different, their changing trends are the same, and the simulation convergence of the monotonic loading is better. Therefore, to reduce the computational cost and achieve better simulation convergence, monotonic loading was used in the simulation in this paper.

4.2 Verification of FE Model

The FE models of PWF2 and PWF3 were constructed, and the skeleton curves obtained from the simulations were compared with those obtained from the experiments, as illustrated in Fig. 13. Upon analysis of the figure, it can be observed that the peak bearing capacity derived from the simulated component closely matches the peak bearing capacity obtained from the experimental test. However, it is worth noting that the simulated components exhibit a higher initial stiffness compared to the experimental results. One plausible explanation for this discrepancy is that the material properties and conditions simulated in the model are idealized, while experiments may encompass uncertainties and potential errors, particularly during concrete placement and reinforcement procedures.

The simulated failure of specimens PWF2 and PWF3 exhibited similar characteristics; therefore, the discussion will focus solely on the simulated failure of PWF2. Fig. 14 illustrates the simulated compressive damage of PWF2. As

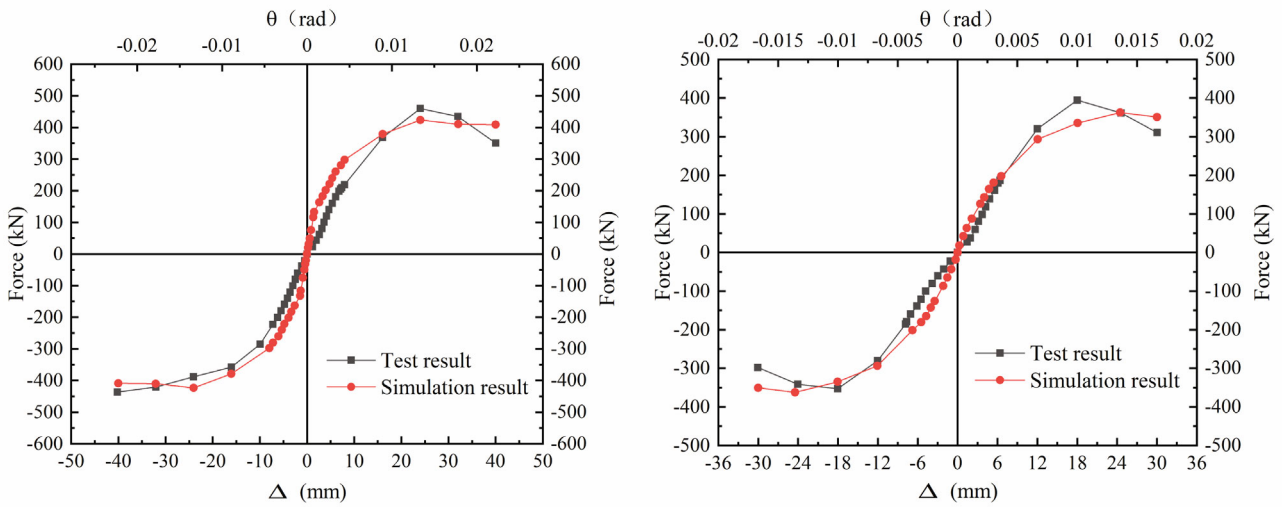

(a)PWF2 (b)PWF3

Fig. 13 Comparison of displacement-force curves of FE simulations and test results

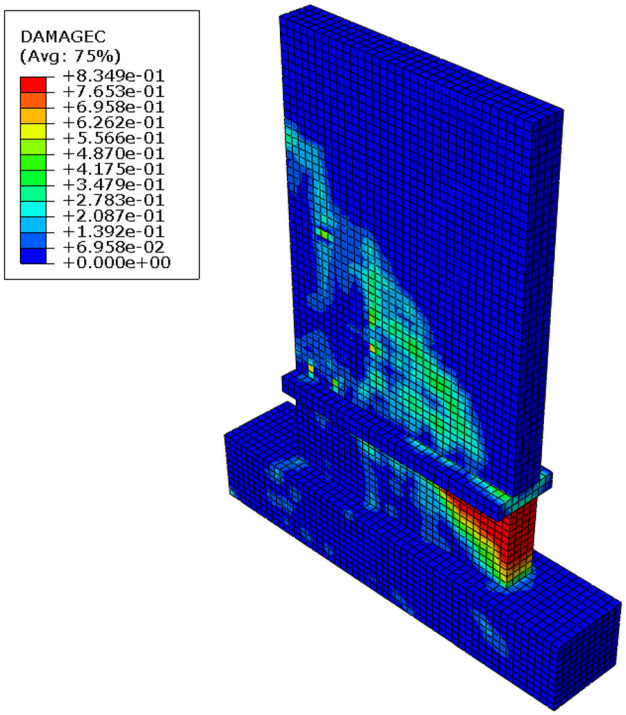

Fig. 14 The simulation failure mode of PWF2

observed in the figure, the crack initially emerges at the corner of the lower PSW, gradually propagating to form a damaged area. The edge of the damaged region forms a 45° angle with the horizontal direction. Meanwhile, during the crack development in the lower PSW, the upper PSW gradually forms an inclined damaged region at a 45° angle relative to the horizontal direction. Notably, the simulation successfully replicates the failure zone at the corner of the PSW and the edge of the floor, which corresponds to the failure zone depicted in Fig. 6 of the experimental results.

Table 6 Comparison of peak lateral shear forces

Type	Peak lateral shear capacity, Vmax (kN)		Gap (%)
	Test(Av)	simulation	
PWF2	453.12	423.53	6.5%
PWF3	373.91	362.42	3.1%

As summarized in Table 6, the discrepancy between the simulated and experimental bearing capacities of the specimens is less than 15%. Furthermore, the failure modes observed in the simulation of PWF2 closely align with the experimental observations. Hence, the model can be regarded as calibrated and serves as a means to validate the accuracy of the experimental results.

4.3 Parametric Analysis

PSWs are subjected to both horizontal and vertical loads in practical applications. The shear span ratio is closely related to the point of application of the horizontal load, while the axial compression ratio is related to the magnitude of the vertical load. Therefore, the axial compression ratio and the shear span ratio are important parameters that affect the seismic properties of PSWs. According to the above modeling methods, parametric analysis of PSWs connected by STRCs was carried out by taking sample PWF2 as the reference, and using the axial compression

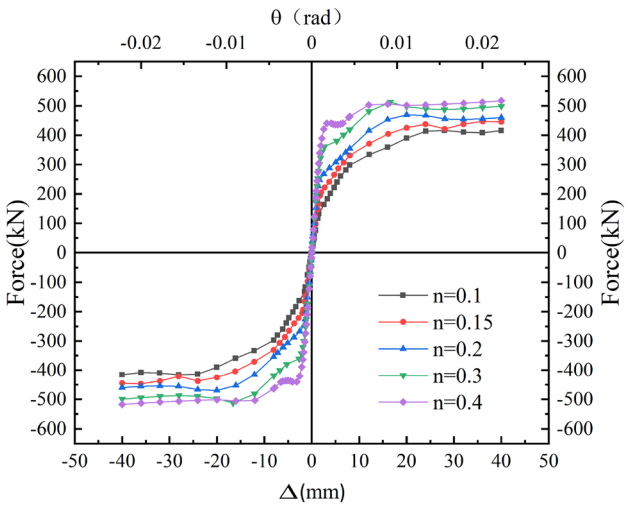

Fig. 15 Comparison of simulation results for specimens with different axial compression ratios

Table 7 Comparison of peak loads on specimen PWF2 with different axial compression ratios

	n = 0.1	n = 0.15	n = 0.2	n = 0.3	n = 0.4
V_{max} (kN)	423.53	439.62	472.67	512.27	507.94
Δ_v (mm)	26.00	25.25	21.59	16.60	12.29

Vmax is the peak lateral shear capacity of PWF2, and Δv is the displacement at which the peak lateral shear capacity is achieved

ratio and the shear span ratio as the variable parameters. PWF2-n-λ means the simulated component obtained under the condition that the axial compressive ratio is n and the shear span ratio is λ.

4.3.1 Axial Compression Ratio

By conducting parametric analysis, the performance of sample PWF2 was obtained at different axial compression ratios, which were 0.15, 0.2, 0.3, and 0.4, respectively.

As shown in Fig. 15 and Table 7, the bearing capacity of PWF2-0.2-1.09 is 13.30% higher than that of PWF2-0.1-1.09, while the bearing capacity of PWF2-0.3-1.09 is 22.79% higher than that of PWF2-0.1-1.09. These findings unequivocally demonstrate a significant increase in the bearing capacity of PWF2 with an increment of the axial compression ratio. However, as the axial compression ratio rises, there is a gradual reduction in the displacement at the peak load of the specimens. Compared to PWF2-0.1-1.09, the displacement at peak load of PWF2-0.2-1.09 decreased by 16.96%, while PWF2-0.3-1.09 exhibited a reduction in displacement of 36.15% at peak load. This indicates that as the axial compression ratio rises, the stiffness of the specimen gradually increases. The bearing capacity of PWF2-0.4-1.09 is similar to that of PWF2-0.3-1.09, illustrating that the bearing capacity of the PSW connected by STRCs will not increase further as the axial compression ratio exceeds 0.4. Therefore, it is suggested that PSWs connected by STRCs should be used with an axial compression ratio no greater than 0.3.

Figure 16 shows the compressive damage of PWF2 with different axial compression ratios. With the increase of axial compression ratio, the damage area of the upper PSW gradually decreases, but the damage area of each specimen develops obliquely first and then gradually changes to vertically. This indicates that the failure mode has not changed and is still the shear-compression failure. The compressed damage area of the lower PSW gradually increases, indicating that as the axial compression ratio rises, the width of the compressed area of the horizontal section of the PSW gradually increases, providing verification for subsequent theoretical calculations.

4.3.2 Shear Span Ratio

By conducting parametric analysis, the performance of specimen PWF2 at shear span ratios of 1.09, 1.34, 1.61, and 1.82 was obtained. As shown in Fig. 17 and Table 8, the bearing capacity of PWF2-0.1-1.34 is 15.98% lower than that of PWF2-0.1-1.09, the bearing capacity of PWF2-0.1-1.61 is 25.29% lower than that of PWF2-0.1-1.09, and the bearing capacity of PWF2-0.1-1.82 is 33.11% lower than that of PWF2-0.1-1.09. This indicates that as the shear span ratio rises, the loading-carrying capacity of the specimen significantly decreases. However, the displacement gradually increases as the peak load is reached. Compared to PWF2-0.1-1.09, the displacement of PWF2-0.1-1.34 at peak load increases by 11.58%, the displacement of PWF2-0.1-1.61 at peak load increases by 25.08%, and the displacement of PWF2-0.1-1.82 at peak load increases by 38.50%. As the shear span ratio rises, the deformation capacity of the specimen gradually increases, which improves the ductility of the specimen to some extent. The peak bearing capacity and displacement at the peak load of the specimen exhibit a stable trend as the shear span ratio varies, indicating that the PSWS connected by STRCs have stable performance in practical engineering applications.

Figure 18 shows the compressive damage of the specimens at various shear span ratios. From the figure, it is observed that as the shear span ratio rises, the degree of damage to the upper shear wall gradually diminishes, the damaged area of the right corner of the lower PSW gradually reduces, and the position of the embedded connector on the tensile side of the upper PSW is damaged. This indicates that as the shear span ratio rises, the shear force

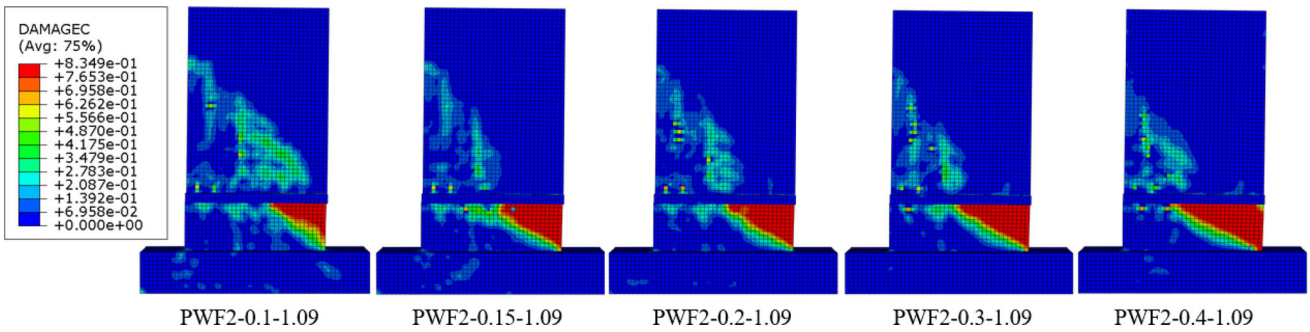

Fig. 16 The compressive damage of PWF2 with different axial compression ratios

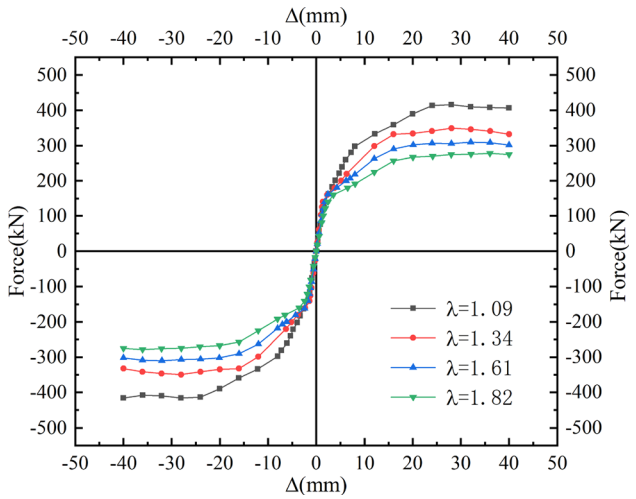

Fig. 17 Comparison of simulation results for specimens with different shear span ratios

Table 8 Comparison of peak loads on specimen PWF2 with different shear span ratios

	λ = 1.09	λ = 1.34	λ = 1.61	λ = 1.82
V_{max} (kN)	423.53	350.53	311.66	279.06
Δ_v (mm)	26.00	29.01	32.52	36.01

borne by the PSW progressively declines, and the bending effect on the PSW increases. This reflects the trend of the PSW failure mode changing from shear-compression failure to bending failure.

5 Lateral Loading Capacity

The calculation method used in this study made some adjustments based on the design method in the Specification [30], by introducing a bending adjustment coefficient λ_i. The calculation model for the lateral loading capacity of PSW connected by STRCs is illustrated in Fig. 19. The lateral loading capacity calculation formulas are shown in equations (4–13).

when $x > 2a_s'$, the area of the compressive zone of concrete is large, and the tensile action of the distributed steel reinforcement is relatively small. Therefore, the tensile effect of the distributed steel reinforcement is not considered.

$$N = A_s' f_s' - A_s \sigma_s + N_c \tag{4}$$

$$M + N\left(h_{w0} - \frac{h_w}{2}\right) = A_s' f_y'\left(h_{w0} - a_s'\right) + M_c \tag{5}$$

$$F_{sw} = \frac{M}{H} \tag{6}$$

$$N_c = \alpha_1 f_c b_w x \tag{7}$$

$$M_c = \alpha_1 f_c b_w x\left(h_{w0} - \frac{x}{2}\right) \tag{8}$$

$$\sigma_s = \begin{cases} f_y \; 2a_s' \le x \le \varepsilon_b h_{w0} \\ \dfrac{f_y}{\varepsilon_b + 0.8}\left(\dfrac{x}{h_{w0}} - \beta_1\right) x > \varepsilon_b h_{w0} \end{cases} \tag{9}$$

$$\varepsilon_b = \frac{\beta_1}{1 + \frac{f_y}{E_s \varepsilon_{cu}}} \tag{10}$$

When $x < 2a_s'$, the area of the compressive zone of concrete is small, and the tensile effect of the distributed steel reinforcement is significant. To take into account the tensile effect of the distributed steel reinforcement, a bending adjustment coefficient ρ_i is introduced. Eq. (5) is replaced by Eq. (11) for calculation.

$$M + N\left(a_s' - \frac{h_w}{2}\right) = A_s f_y (h_{w0} - a_s) + \sum_{i=1}^{n} M_i \tag{11}$$

$$\rho_i = \frac{h_{wi}}{h_{w0} - a_s} \tag{12}$$

$$M_i = f_{yi} A_{si} h_{wi} \lambda_i \tag{13}$$

N represents the vertical load applied to the prestressed wall; A_s and A_s' represent the cross-sectional areas of the tensile steel reinforcement and the compression steel reinforcement, respectively; f_y and f_y' represent the yield

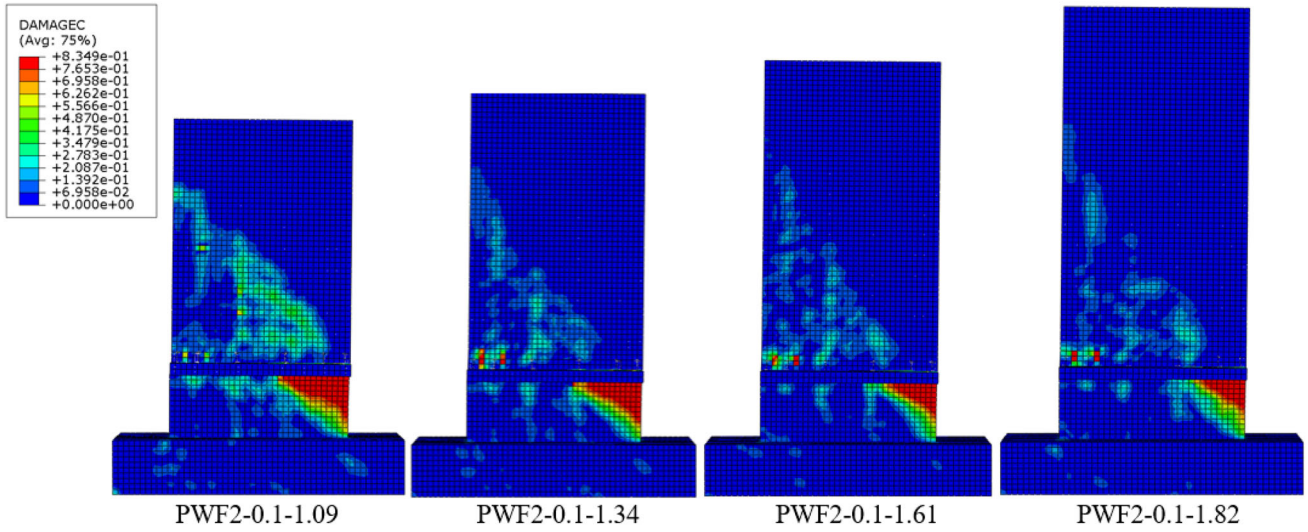

Fig. 18 Compressive damage of specimen PWF2 at different shear span ratios

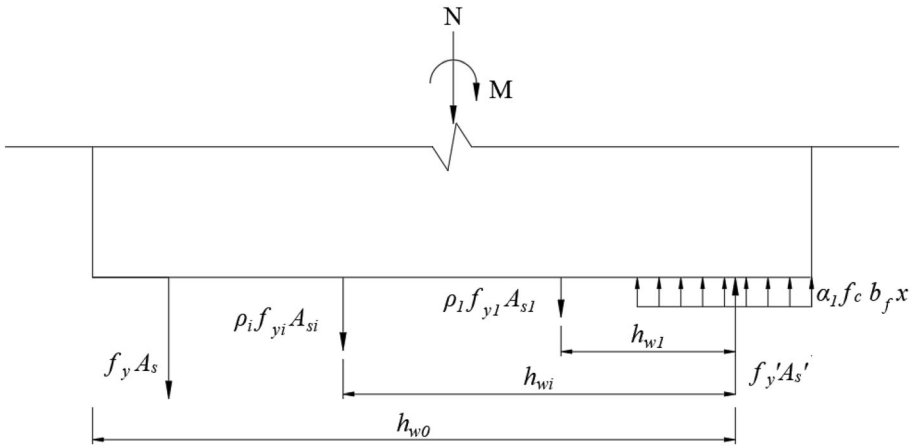

Fig. 19 Calculation model of lateral loading capacity

Table 9 Comparison of test/simulated values with calculated values of specimens

specimen	n	λ	F_p/kN	F_{sw}/kN	$(F_{sw}$-$F_p)$ /F_p
PWF2	0.1	1.09	453.12	451.19	-0.46%
PWF3	0.1	1.09	373.91	417.85	11.75%
PWF2-0.1-1.09	0.1	1.09	415.80	451.19	8.51%
PWF2-0.15-1.09	0.15	1.09	439.62	491.88	11.89%
PWF2-0.2-1.09	0.2	1.09	472.67	531.70	12.79%
PWF2-0.3-1.09	0.3	1.09	512.27	610.88	19.25%
PWF2-0.1-1.34	0.1	1.34	350.53	369.35	5.37%
PWF2-0.1-1.61	0.1	1.61	311.66	312.63	0.31%
PWF2-0.1-1.82	0.1	1.82	279.06	271.02	-2.88%

n is the axial compression ratio, λ is the shear span ratio, F_p is the experimental or simulated value, and F_{sw} is the formula calculated value

strengths of steel reinforcement in tension and compression, respectively.; α_1 is the stress coefficient of the equivalent rectangular stress block; f_c denotes the design value of the axial compressive strength of concrete[24]; x denotes the height of the compressed zone of concrete, h_{w0} is the effective height of the PSW section, $h_{w0} = h_w - a_s'$; h_w is the height of the PSW section; a_s and a_s' represent the distances from the centroid of the tensile steel reinforcement region and the compressive steel reinforcement region to the edges of the PSW cross-section, respectively; b_w is the width of the PSW; E_s is the elastic modulus of concrete; ε_b denotes boundary relative height of compression zone.

Table 9 presents a comparison of the test/simulated values of the lateral loading capacity with the calculated values of the lateral loading capacity for PSW. The proposed formula tends to overestimate the lateral loading capacity of the PSW when the axial compression ratio is

relatively large, while it provides accurate results when the axial compression ratio is relatively small. For specimens with different shear span ratios, the proposed formula provides accurate results. The calculation results have a high correlation with most of the test/simulation results, with errors of most specimens within 15%. Therefore, the calculation method can be used to evaluate the lateral loading capacity of PSW connected by STRC.

Based on the experimental results and finite element simulation results, the lateral bearing capacity calculation formula refers to the existing standard formula, discusses the two different stress states of the PSW, and effectively predicts the lateral bearing capacity of the PSW by introducing the distributed reinforcement bending moment adjustment coefficient, providing a reference for the design of subsequent new PSWs. From the perspective of finite element simulation results and lateral bearing capacity calculation, when the axial compression ratio of this new type of PSW exceeds 0.3, the bearing capacity no longer rises, but the displacement of the peak load gradually decreases. Therefore, the recommended axial compression ratio of this new type of PSW does not exceed 0.3. As the shear span ratio increases, the bearing capacity of the specimen gradually decreases, so the recommended shear span ratio does not exceed 1.61.

6 Conclusion

Three PSW specimens were tested under cyclic loading, one connected by grouted sleeve connectors and two connected by STRCs. The performance of the PSWs was evaluated in terms of failure mode, load-carrying capacity, stiffness, energy dissipation, and ductility. Additionally, the influence of parameters such as axial compression ratio and shear span ratio on the performance of PSWs was investigated through FE simulations. Finally, a novel calculation method for the lateral loading capacity of this type of PSW was proposed. The conclusions derived from this study are as follows:

1. The prefabricated PSWs connected by STRCs exhibited similar load-carrying capacity to the PSWs connected by grouted sleeve connectors. The average peak load in both positive and negative directions for PWF1 and PWF2 was approximately 450 kN, indicating minimal differences in load capacity. Furthermore, the threaded rod connectors showed no significant signs of damage or failure. The STRC is capable of effectively transferring loads between PSWs and can serve as a reliable connection for PSWs.
2. PSWs connected by STRCs exhibit good energy dissipation capacity and ductility. The energy dissipation capacity of PSWs connected by STRCs is similar to that of PSWs connected by grouting sleeves, but PSWs connected by STRC demonstrate better ductility and deformation capacity. These findings indicate that PSWs connected by STRCs possess good seismic performance.
3. The enhancement of the axial compression ratio results in increased load-carrying capacity and stiffness for PSW connected by STRC. However, as the axial compression ratio rises, the ductility of the PSW gradually diminishes. When the axial compression ratio exceeds 0.3, the bearing capacity of the PSW no longer increases. Based on the parameter analysis results, it is advisable to maintain the axial compression ratio within the range of 0.2 to 0.3 and avoid exceeding 0.4.
4. As the shear span ratio increases, the deformation capacity of the PSW gradually increases while its bearing capacity decreases. As the shear span ratio rises, the failure mode of PSW exhibits a trend transitioning from shear-compression failure to bending failure.
5. The lateral loading capacity calculation method proposed in this paper can predict the lateral loading capacity of this new type of PSW with a relatively high degree of accuracy, providing a foundation for subsequent research on PSWs.

Author contributions Tianxi Cheng made the acquisition, analysis, interpretation of data, finite element parameter analysis and derivation of the calculation equations. Shuo Li made interpretation of data.and derivation of the calculation equations. Yunyan Bai made the analysis. Peijun Wang revised the work critically for important intellectual content. Qi Wang revised the interpretation of data. Jie Song made interpretation of data. Mei Liu made substantial contributions to the conception and design of the work.

Funding This work is financially supported by the National Natural Science Foundation of China [grant number 52078280, grant number 52127814].

Data availability The datasets used or analyzed during the current study are available from the corresponding author on reasonable request.

Code availability Not applicable.

Declarations

Conflict of interest We declare that we have no financial and personal relationships with other people or organizations that can inappropriately influence our work, and there is no professional or other personal interest of any nature or kind in any product, service and/or company that could be construed as influencing the position presented in, or the review of, the manuscript entitled, "Study on seismic performance of precast shear wall structure connected by sleeve and threaded rod connectors".

References

1. VanGeem M (2006) Achieving sustainability with precast concrete. PCI J 51(1):42–61
2. Yee A (2001) Social and environmental benefits of precast concrete technology. PCI J 46(3):14–9
3. Karaton M, Osmanlı ÖF, Gülşan ME (2021) Investigation of uncertainties in nonlinear seismic analysis of the reinforced concrete shear walls. Int J Civ Eng 19:301–318
4. Singhal S, Chourasia A, Chellappa S, Parashar J (2019) Precast reinforced concrete shear walls: state of the art review. Struct Concr 20(3):886–898
5. Fang Q, Qiu H, Sun J et al (2022) Experimental study on shear performance of steel-concrete composite bolted connectors in precast concrete shear walls. Int J Civ Eng 20:445–459
6. Hutchinson R, Rizkalla S, Lau M et al (1991) Horizontal post-tensioned connections for precast concrete load bearing shear wall panels. PCI J 36(6):64–76
7. Soudki K, Rizkalla S, Daikiw R (1995) Horizontal connections for precast concrete shear walls subjected to cyclic deformations part 2: prestressed connections. PCI J 40(5):82–96
8. Xue W, Huang Q, Gu X et al (2022) Hysteretic behavior of precast concrete shear walls with steel sleeve-corrugated metallic duct hybrid connections. Struct 38:820–831
9. Peng Y, Qian J, Wang Y (2016) Cyclic performance of precast concrete shear walls with a mortar–sleeve connection for longitudinal steel bars. Mater Struct 49(6):2455–2469
10. Xu G, Wang Z, Wu B et al (2017) Seismic performance of precast shear wall with sleeves connection based on experimental and numerical studies. Eng Struct 150:346–358
11. Zhi Q, Guo Z, Xiao Q et al (2017) Quasi-static test and strut-and-tie modeling of precast concrete shear walls with grouted lap-spliced connections. Constr Build Mater 15:190–203
12. Qu X, Xie Y, Sun Y et al (2023) Study of mechanical properties of grouting defective sleeve. Struct 48:1128–1140
13. Xiao S, Wang Z, Li X et al (2021) Study of effects of sleeve grouting defects on the seismic performance of precast concrete shear walls. Eng Struct 236:111833
14. Shemie M (1973) Bolted connections in large panel system buildings. PCI J 18(1):27–33
15. Cheng B, Cai Y, Looi D (2021) Experiment and numerical study of a new bolted steel plate horizontal joints for precast concrete shear wall structures. Struct 32:760–777
16. Hofheins C, Reaveley L, Pantelides C (2002) Behavior of welded plate connections in precast concrete panels under simulated seismic loads. PCI J 47(4):122–133
17. Fu Y, Fan G, Tao L (2022) Seismic behavior of prefabricated steel reinforced concrete shear walls with new type connection mode. Struct 37:483–503
18. Semelawy M, Soliman A, Damatty A (2015) Novel anchor-jointed precast shear wall: testing and validation. Proc Inst Civil Eng Struct Build 168(4):263–274
19. Semelawy M, Soliman A, Damatty A (2017) Finite-element analysis of anchor-jointed precast structural wall system. Proc Inst Civil Eng Struct Build 170(8):543–554
20. Guo W, Zhai Z, Yu Z et al (2019) Experimental and numerical analysis of the bolt connections in a low-rise precast wall panel structure system. Adv Civ Eng. https://doi.org/10.1155/2019/7594132
21. Li W, Gao H, Xiang R et al (2021) Experimental study of seismic performance of precast shear wall with a new bolt-plate connection joint. Struct 34:3818–3833
22. Han Q, Wang D, Zhang Y et al (2020) Experimental investigation and simplified stiffness degradation model of precast concrete shear wall with steel connectors. Eng Struc 220:110943
23. Naserpour A, Fathi M, Dhakal RP (2022) Demountable shear wall with rocking boundary columns for precast concrete buildings in high seismic regions. Struct 41:1454–1474
24. GB T 50081–2019 (2019) Standard for test methods of concrete physical and mechanical properties. China Building Industry Press, Beijing
25. GB50010-2010 (2010) Code for design of concrete structures. China architecture and building press, Beijing
26. JG T 408–2019 (2019) Cementitious grout for sleeve of rebar splicing. China standards press, Beijing
27. GB T 228.1-2010 (2010) Metallic materials—tensile testing—part 1: method of test at room temperature. Architecture and building press, Beijing
28. JGJ T 101–2015 (2015) Specification for seismic test of buildings. China building industry press, Beijing
29. Guo Z (1999) Principle of reinforced concrete. Tsinghua University Press, Beijing
30. TCECS795-2021 (2021) Technical specification for monolithic assembled concrete shear wall structure with non-connected vertical distribution reinforcement. China Architecture & Building Press, Beijing